# An autoinhibited state of 53BP1 revealed by small molecule antagonists and protein engineering

Gaofeng Cui[1,*], Maria Victoria Botuyan[1,*], Pascal Drané[2,*], Qi Hu[1], Benoît Bragantini[1], James R. Thompson[3], David J. Schuller[4], Alexandre Detappe[5], Michael T. Perfetti[6], Lindsey I. James[6,7], Stephen V. Frye[6,7], Dipanjan Chowdhury[2] and Georges Mer[1,8,#]

*Equal contributions

[#]Correspondence: mer.georges@mayo.edu

[1]Department of Biochemistry and Molecular Biology, Mayo Clinic, Rochester, MN, USA

[2]Department of Radiation Oncology, Dana-Farber Cancer Institute, Boston, MA, USA

[3]The Hormel Institute, University of Minnesota, Austin, MN, USA

[4]Cornell High Energy Synchrotron Source, Cornell University, Ithaca, NY, USA

[5]Institut de Cancérologie Strasbourg Europe, Strasbourg, France

[6]Center for Integrative Chemical Biology and Drug Discovery, Division of Chemical Biology and Medicinal Chemistry, UNC Eshelman School of Pharmacy, University of North Carolina at Chapel Hill, Chapel Hill, NC, USA

[7]Lineberger Comprehensive Cancer Center, University of North Carolina at Chapel Hill School of Medicine, Chapel Hill, NC, USA

[8]Department of Cancer Biology, Mayo Clinic, Rochester, MN, USA

**Abstract**

The recruitment of 53BP1 to chromatin, mediated by its recognition of histone H4 dimethylated at lysine 20 (H4K20me2), is important for DNA double-strand break repair. Using a series of small molecule antagonists, we demonstrate a conformational equilibrium between an open and a pre-existing lowly populated closed state of 53BP1 in which the H4K20me2 binding surface is buried at the interface between two interacting 53BP1 molecules. In cells, these antagonists inhibit the chromatin recruitment of wild type 53BP1, but do not affect 53BP1 variants unable to access the closed conformation despite preservation of the H4K20me2 binding site. Thus, this inhibition operates by shifting the conformational equilibrium toward the closed state. Our work therefore identifies an auto-associated form of 53BP1 — autoinhibited for chromatin binding — that can be stabilized by small molecule ligands encapsulated between two 53BP1 protomers. Such ligands are valuable research tools to study the function of 53BP1 and have the potential to facilitate the development of new drugs for cancer therapy.

## Introduction

The DNA damage response protein 53BP1 (p53-binding protein 1) influences the cell cycle dependency of DNA double-strand break (DSB) repair pathway selection. During G1 phase of the cell cycle, 53BP1 inactivates DSB repair by homologous recombination (HR) and promotes non-homologous end joining (NHEJ). These activities are balanced by the BRCA1-BARD1 E3 ubiquitin ligase, which promotes HR in post-replicative chromatin[1-4], possibly by reshuffling the chromatin localization of 53BP1 during the S and G2 phases[5]. Both 53BP1 and BRCA1-BARD1 recognize DSB-dependent mono-ubiquitylation of histone H2A K15 (H2AK15ub) in chromatin[6-11]. The localization of 53BP1 to chromatin also requires that it binds histone H4 di-methylated at K20 (H4K20me2) via a tandem Tudor domain ($53BP1^{TT}$) (**Fig. 1a**) [12,13], while BRCA1-BARD1 recruitment requires unmethylated H4K20 recognized by an Ankyrin repeat domain in BARD1[10,11,14]. Our understanding of how 53BP1 and BRCA1-BARD1 contribute to DNA repair pathway selection is incomplete. Investigations of the antagonistic roles of 53BP1 and BRCA1-BARD1 have mostly relied on the identification of separation-of-function mutations. Here, we explore the utility of small molecule ligands that antagonize the recruitment of 53BP1 to chromatin. Blocking the H4K20me2 recognition site of $53BP1^{TT}$ is a prospective means of preventing binding to chromatin. We show that a series of water-soluble small molecules targeting the methyl-lysine binding cavity in $53BP1^{TT}$ function by stabilizing a previously unknown lowly populated autoinhibited homodimeric state of $53BP1^{TT}$ in which the histone binding surface of H4K20me2 is buried within the protomeric interface. Using these small molecule antagonists and functional 53BP1 constructs consisting of both wild type and mutants engineered to block auto-association via the tandem Tudor domain while retaining chromatin binding capability, we then demonstrate that the autoinhibited state of 53BP1 exists in cells as

well. This work paves the way for further exploration of 53BP1 function and modes of action and provides insight for the design of more potent and selective 53BP1 antagonists.

## Results

### A 53BP1 tandem Tudor homodimer encapsulates small molecules in solution

We previously identified a fragment-like small molecule, UNC2170, that binds the aromatic methyl-lysine binding cage of $53BP1^{TT}$ with a dissociation constant ($K_d$) of 22 ± 2.5 μM and is competitive with an H4K20me2 peptide[15]. Intriguingly, in a crystal structure of UNC2170 bound to $53BP1^{TT}$, the small molecule ligand was in contact with two $53BP1^{TT}$ molecules. Our structural characterization of $53BP1^{TT}$ in complex with the related compounds UNC2991 ($K_d$ = 3.9 ± 0.4 μM), UNC3351 ($K_d$ = 6.8 ± 0.4 μM) and UNC3474 ($K_d$ = 1.0 ± 0.3 μM) (**Extended Data Fig. 1a)** revealed a similar three-dimensional (3D) arrangement wherein each ligand not only blocked the methyl-lysine binding site but was encapsulated in a cavity generated by two $53BP1^{TT}$ molecules (**Fig. 1b,c and Table 1**). This consistent burial of the histone binding surface of $53BP1^{TT}$ by dimerization was unexpected. While crystallization could drive $53BP1^{TT}$ homodimerization as has been shown for several other systems[16], that all four 3D structures were comparable despite differing crystallization conditions and space groups suggested that some $53BP1^{TT}$ dimer may also exist in solution, even though all previous NMR spectroscopy studies only reported a monomeric state for $53BP1^{TT}$ (**Fig. 1d**) [12,13,17-19]. Since the homodimerization interface in the crystal structures buries the histone binding surface of $53BP1^{TT}$ (**Fig. 1c,d**), such a conformation would be autoinhibitory for chromatin binding. Small molecules that stabilize this autoinhibited state of $53BP1^{TT}$ — including in the context of full-length 53BP1 — could

potentially inhibit 53BP1 recruitment to DSBs.

Using analytical ultracentrifugation (AUC) sedimentation velocity, we showed that addition of UNC3474 to $53BP1^{TT}$ caused a change in sedimentation coefficient that was consistent with the dimerization of $53BP1^{TT}$ (**Fig. 2a**). Moreover, changes in small-angle X-ray scattering (SAXS) [20] data upon $53BP1^{TT}$-UNC3474 complex formation agreed well with $53BP1^{TT}$ homodimerization, including an increase in the radius of gyration (**Extended data Fig. 1b**). As a control, we used the small molecule UNC1118, which interacts with $53BP1^{TT}$ via a dimethyl-lysine-mimicking pyrrolidine-piperidine motif ($IC_{50}$ = 7.4 ± 1.1 μM) as we previously showed[21]. We confirmed this interaction by measuring a $K_d$ of 8.5 ± 0.9 μM (**Extended data Fig. 1c**). We hypothesized that UNC1118 would be too large to be buried within a $53BP1^{TT}$ homodimer. Addition of UNC1118 produced SAXS data similar to those of $53BP1^{TT}$ alone, indicating that UNC1118 is not capable of binding the homodimer (**Extended data Fig. 1b**). *Ab initio* derivation of molecular envelopes from the SAXS scattering curves of $53BP1^{TT}$ and $53BP1^{TT}$-UNC3474 disclosed changes consistent with $53BP1^{TT}$ homodimerization in the presence of UNC3474 (**Extended data Fig. 1b**).

Investigation by solution NMR spectroscopy also revealed the dimeric conformation first identified in our $53BP1^{TT}$ crystal structures. Titration of UNC2170, UNC2991, UNC3351 and UNC3474 into $^{15}N$-labeled $53BP1^{TT}$ led to changes in several signal positions in the $^{1}H$-$^{15}N$ heteronuclear single quantum coherence (HSQC) NMR spectrum of $53BP1^{TT}$ indicative of slow exchange on the chemical shift time scale (**Extended data Fig. 2a**). These chemical shift perturbations were more extensive than could be expected for just the small molecule binding surface and also mapped to amino acids located at the $53BP1^{TT}$ dimer interface in our crystal structures (**Extended data Fig. 2b,c**). Several of the $53BP1^{TT}$ residues that are close to the small

molecule binding site had two different NMR signals. This is consistent with loss of symmetry observed in our crystal structures, allowing interactions by each of the two 53BP1$^{TT}$ protomers with a different "side" of the bound small molecule (**Fig. 1c,d**, **Fig. 2b, Extended data Fig. 2b**). NMR relaxation data further supported an increase in molecular weight consistent with 53BP1$^{TT}$ dimerization in the presence of UNC3474 as can be seen from an increase in R2 relaxation rates for the 53BP1$^{TT}$-UNC3474 complex (**Extended data Fig. 3a**). In comparison, binding of UNC1118 to 53BP1$^{TT}$ had no marked effect on the relaxation rates of 53BP1$^{TT}$ (**Extended data Fig. 3a**).

In addition, for the lowest affinity compound, UNC2170, a slow exchange could be quantified between each of the two protomers in the 53BP1$^{TT}$ dimer with interconversion rates of 1.7 $s^{-1}$ and 1.2 $s^{-1}$ at 25 °C using 2D longitudinal $^{1}H$-$^{15}N$-heteronuclear ZZ-exchange NMR spectroscopy[22-24] (**Fig. 2c**). This exchange likely reflects the interconversion between the two 53BP1$^{TT}$ protomers binding the two different "sides" of the ligand. In the presence of the other compounds, which have higher affinity than UNC2170 for 53BP1$^{TT}$, the exchange between the two 53BP1$^{TT}$ protomers was too slow to be quantifiable under the same conditions. Taken together, our data demonstrate that like in the crystal structures, the small molecules are buried at the interface of a 53BP1$^{TT}$ homodimer in solution.

**Identification of a weakly populated homodimeric state of 53BP1 tandem Tudor domain *in vitro***

The small molecules may cause 53BP1$^{TT}$ to homodimerize or they could stabilize a weakly populated, pre-existing 53BP1$^{TT}$ homodimer that evaded prior detection. This distinction is important. If auto-association, which buries the H4K20me2 binding surface in 53BP1$^{TT}$, also

occurs in the context of full-length 53BP1, then 53BP1 may employ autoinhibition as a regulatory mechanism for chromatin recruitment.

In our crystal structures (**Fig. 1b**), W1495 of $53BP1^{TT}$ is essential for small molecule binding and it also contributes to the $53BP1^{TT}$ homodimer interface. Several other inter-$53BP1^{TT}$ contacts in the crystal structures, however, are distant from the ligand binding site and might be exploited to disrupt dimer formation while not affecting binding of the small molecules. Such inter-$53BP1^{TT}$ contacts include the hydrophobic interactions between Y1552 and L1518, and salt bridges involving the E1549-R1583, D1550-R1490, and D1550-K1505 pairs (**Fig. 3a**). To test the possibility of a pre-existing $53BP1^{TT}$ homodimer, we created a $53BP1^{TT}$ mutant ($53BP1^{TT}$-PN) in which E1549 and D1550 were replaced by a proline and an asparagine, respectively, to introduce a 3D structure-preserving β-turn in $53BP1^{TT}$. These mutations eliminate the six salt bridges at the $53BP1^{TT}$ dimer interface as mentioned above but do not affect the small molecule-binding surface. We verified that the structural integrity of $53BP1^{TT}$-PN was preserved by determining a 2.20 Å resolution crystal structure of this protein variant (**Fig. 3b, Table 1**). The backbone dynamic properties of wild type $53BP1^{TT}$ and $53BP1^{TT}$-PN were quite similar as shown using NMR relaxation measurements (**Extended Data Fig. 3b**). Like wild type $53BP1^{TT}$, $53BP1^{TT}$-PN bound dimethylated histone (H4K20me2) and dimethylated p53 (p53K382me2) peptides as expected[12,13,18,19] (**Fig. 3c**), but unlike WT $53BP1^{TT}$, $53BP1^{TT}$-PN did not interact with UNC2170, UNC2991 or UNC3474 (**Fig. 3d**). There were no changes in the $^{1}H$-$^{15}N$ HSQC spectra of $^{15}N$-labeled $53BP1^{TT}$-PN after addition of up to 4-fold molar excess of each of these small molecules (**Fig. 3d**). As a control, we also examined the interaction of $53BP1^{TT}$-PN with the compound UNC1078, which like UNC1118, is a larger molecule that interacts with $53BP1^{TT}$ as a monomer via an established dimethyl-lysine-mimicking pyrrolidine-piperidine motif and

does not cause dimerization (**Extended Data Fig. 4a**). As expected, 53BP1$^{TT}$-PN also bound UNC1078 (**Fig. 3c**). The most likely interpretation for the absence of interaction of 53BP1$^{TT}$-PN with UNC2170, UNC2991 and UNC3474 is that these small molecules do not cause 53BP1$^{TT}$ dimerization directly. Instead, they only bind to and stabilize a pre-existing 53BP1$^{TT}$ homodimer population, shifting the equilibrium toward homodimer. When overlaid, the $^{1}$H-$^{15}$N HSQC spectra of wild type 53BP1$^{TT}$ and 53BP1$^{TT}$-PN showed small chemical shift changes that map to the inter-53BP1$^{TT}$ interface in 53BP1$^{TT}$-UNC3474. This is further evidence for a preexisting small population of 53BP1$^{TT}$ homodimer that is eliminated in 53BP1$^{TT}$-PN (**Extended Data Fig. 4b**).

As an added test of this binding mechanism, we designed a disulfide-crosslinked[25] 53BP1$^{TT}$ variant that assembles into a stable dimer in the absence of a ligand. Using the software Disulfide by Design[26] applied to the highest resolution structure in Table 1 (Protein Data Bank entry: 6MXY), we selected E1549 and E1567 for replacement by cysteines. These mutations readily linked two 53BP1$^{TT}$ molecules covalently into a homodimer (53BP1$^{TT}$-CC) via formation of two intermolecular C1549-C1567 disulfide bridges as shown using AUC sedimentation velocity (**Fig. 4a**). A low resolution (3.8 Å) model of 53BP1$^{TT}$-CC derived from X-ray crystallography data was sufficient to demonstrate that both protomers were arranged similarly as wild type 53BP1$^{TT}$ bound to our small molecules with a root-mean-square deviation for backbone atoms of 0.94 Å. (**Fig. 4b, Table 1**). Using NMR spectroscopy, we independently verified that 53BP1$^{TT}$-CC mimicked the homodimeric state of 53BP1$^{TT}$ bound to UNC3474 (**Fig. 4c**). Noticeably, the addition of UNC3474 led to the splitting of several NMR signals in the $^{1}$H-$^{15}$N HSQC spectra of 53BP1$^{TT}$-CC. Addition of the reducing agent dithiothreitol (DTT) changed 53BP1$^{TT}$-CC to a monomeric state as expected which, like 53BP1$^{TT}$-PN, had no affinity for

UNC3474 (**Fig. 4c**). We therefore created 53BP1$^{TT}$ variants that can be switched on and off *in vitro* for ligand binding. These mutations may be useful for the study of a longer, functional 53BP1 in cells.

**Demonstration of an autoinhibited state of 53BP1 in cells using a small molecule ligand**

After showing that an autoinhibited state of 53BP1 exists *in vitro* and can be stabilized by small molecules, we next evaluated the effect of small molecule UNC3474 on 53BP1 localization to chromatin in cells in response to DNA damage. We first reconstituted mammalian U2OS cell lines to stably express a minimal segment of 53BP1 protein — the oligomeric foci-forming region (53BP1$^{FFR}$: residues 1220-1711) (**Fig. 1a**) — that contains the tandem Tudor domain and is necessary for DNA damage site recruitment[7,27-29] (**Fig. 5a**). Cells were generated that express wild type (WT) 53BP1$^{FFR}$ and the mutants 53BP1$^{FFR}$-PN and 53BP1$^{FFR}$-CC.

Using immunofluorescence microscopy, we observed robust formation of ionizing radiation-induced foci (IRIF) after cell exposure to 1 Gy of X-ray radiation for WT 53BP1$^{FFR}$, 53BP1$^{FFR}$-PN and 53BP1$^{FFR}$-CC (**Fig. 5b**). Upon treatment with different concentrations of UNC3474, IRIF formation was inhibited in a dose-dependent manner for WT 53BP1$^{FFR}$ (**Fig. 5b,c**). Under identical experimental conditions, there was no significant change in 53BP1$^{FFR}$-PN and 53BP1$^{FFR}$-CC IRIF upon treatment with UNC3474 (**Fig. 5c**). The Ser139-phosphorylated histone H2A.X (γH2A.X) IRIF served as a marker for DNA damage in these experiments (**Fig. 5d**). As we showed *in vitro*, 53BP1$^{TT}$-PN and reduced-state 53BP1$^{TT}$-CC cannot dimerize and are thus insensitive to UNC3474 and to the related, lower affinity compounds UNC2170 and UNC2991 (**Fig. 3d**). 53BP1$^{FFR}$-CC is expected to be in a reduced state in mammalian cells owing to the reductive nuclear environment[30,31] and activation of antioxidant enzymes in

response to ionizing radiation[32]. 53BP1$^{FFR}$-CC would therefore be predicted to behave like 53BP1$^{FFR}$-PN. These results show that UNC3474 inhibits the recruitment of 53BP1 to DSBs by stabilizing a pre-existing autoinhibited state of 53BP1 in cells. We have therefore demonstrated the existence of an autoinhibited form of 53BP1 with a small molecule ligand used as a chemical probe.

**Discussion**

Numerous proteins harbor a methyl-lysine binding cage like that of 53BP1[33], making the development of ligands that are selective for a single methyl-lysine reader protein challenging[34]. Nevertheless, a few selective ligands for methyl-lysine readers have been developed[35]. For example, UNC1215 is a bivalent chemical probe that potently binds chromatin-interacting transcriptional repressor L3MBTL3 by inducing the formation of a 2:2 protein:ligand complex[36]. In a radically different mechanism, UNC3474 and the structurally related small molecules we characterized here stabilize a pre-existing auto-associated form of 53BP1$^{TT}$ with a 2:1 protein:ligand stoichiometry. Our studies revealed that these compounds bind the aromatic cage of 53BP1$^{TT}$, but only when 53BP1$^{TT}$ homodimers exist. We showed that 53BP1$^{TT}$ constructs engineered to prevent auto-association — while preserving the ligand binding cage — have no affinity for the small molecule ligands, and yet, they bind H4K20me2 and p53K382me2 like wild type 53BP1$^{TT}$.

Using these small molecules as chemical probes, we demonstrated that a pre-existing autoinhibited form of 53BP1 exists in cells. The function of autoinhibited 53BP1 is not yet understood. Nevertheless, we can speculate that this state may be stabilized *in vivo* under certain conditions to regulate the activity of 53BP1. We note that full-length 53BP1 and 53BP1$^{FFR}$ are

constitutive homomultimers[37] via an oligomerization domain of unknown structure located upstream from the tandem Tudor domain (**Fig. 1a**) [38-41]. In the context of oligomeric 53BP1$^{FFR}$, the auto-association of 53BP1$^{TT}$ and its stabilization by small molecule ligands reported here are likely amplified by the avidity effect, providing a unique and highly specific means of inhibiting the interaction of 53BP1 with chromatin. In future studies, we will explore the influence of these ligands on other functions of 53BP1 reliant upon its interactions with the regulatory protein TIRR[28,40,42-44] and K382me2-carrying p53 tumor suppressor[18,45]. Ligand-binding to 53BP1 is predicted to disrupt these interactions.

Our work is expected to facilitate the structure-based design of improved ligands that are more potent in stabilizing the 53BP1$^{TT}$ homodimer and in inhibiting 53BP1 in cells. Such molecules would help further dissect aspects of 53BP1 modes of action. These molecules could also be used to promote DNA repair by homologous recombination and thereby increase the effectiveness of genome editing using CRISPR-Cas9 or related systems[46,47]. Furthermore, pharmacological inhibition of 53BP1 is of interest for brain cancer therapy[48]. For example, silencing of the 53BP1 gene sensitizes glioma cells to ionizing radiation by prolonging cell cycle arrest and increasing apoptosis[49]. The expression of 53BP1 is increased in temozolomide-resistant glioblastoma cells and depletion of 53BP1 increases the potency of temozolomide against glioblastoma[50]. Potent and selective inhibitors of 53BP1 could therefore serve as lead compounds for drug development.

## Methods

### Protein purification

The tandem Tudor domain of 53BP1 ($53BP1^{TT}$, residues 1481-1603) was purified as previously described[12]. The W1495A, E1549P/D1550N ($53BP1^{TT}$-PN) and E1549C/E1567C ($53BP1^{TT}$-CC) mutants were similarly prepared. The p53K382me2 (residues 377-386) peptide was purchased from GenScript while the $H4K_{C}20me2$ (residues 12-25) was prepared from expression in *E. coli* with chemical installation of a dimethyl-lysine analog as previously reported[51-53]. The two peptides were purified by reversed-phase chromatography using a preparative C18 column (Phenomenex).

**Preparation of small compounds**

The small molecule ligands UNC2170, UNC2991, UNC3351, and UNC3474 and control ligands UNC1078 and UNC1118 were synthesized as described previously[15,21].

**Nuclear magnetic resonance (NMR) spectroscopy**

All NMR data were collected at 25 °C on a 700 MHz Bruker Avance III spectrometer equipped with a cryoprobe. Data were processed and analyzed with NMRPipe[54] and NMRViewJ[55,56].

For the backbone resonance assignments of $53BP1^{TT}$ in the presence of UNC3474, we prepared samples of 1 mM $^{15}N$- and $^{15}N$,$^{13}C$-labeled WT $53BP1^{TT}$ with 5-fold molar excess of non-labeled UNC3474 in 25 mM sodium phosphate, pH 7.0, 100 mM NaCl, 1.5 mM $NaN_3$, 0.3 mM DSS, 90% $H_2O$/10% $D_2O$. A series of standard NMR experiments including 2D $^{1}H$-$^{15}N$ HSQC and $^{1}H$-$^{13}C$ HSQC and 3D HNCACB, CBCA(CO)NH, HNCO, HN(CA)CO, HBHA(CO)NH, $^{15}N$-edited NOESY-HSQC and $^{13}C$-edited NOESY-HSQC were recorded[57].

To probe chemical shift perturbations, $^{1}H$-$^{15}N$ HSQC spectra were acquired on the

following samples: 0.2 mM $^{15}$N-labeled 53BP1$^{TT}$ WT and 53BP1$^{TT}$-PN in 25 mM sodium phosphate, pH 7.0, 1.5 mM $NaN_3$, 0.3 mM DSS, 90% $H_2O$/10% $D_2O$ free and incrementally titrated with various non-labeled inhibitors (UNC1078, UNC1118, UNC2170, UNC2991, UNC3474), as well as with H4K$_C$20me2 and p53K382me2 peptides. Chemical shift perturbations (Δδ) were calculated using the equation:

$$\Delta\delta = \sqrt{(\Delta N/5)^2 + (\Delta H)^2}$$

where ΔN and ΔH are the corresponding differences in $^{15}$N and $^{1}$H chemical shifts between the bound and free forms of 53BP1.

The NMR relaxation measurements were carried out with 1 mM $^{15}$N-labeled 53BP1$^{TT}$, 53BP1$^{TT}$-PN, and $^{15}$N-labeled 53BP1$^{TT}$ in the presence of saturating amounts of UNC3474 and UNC1118 in 25 mM sodium phosphate, pH 7.0, 100 mM NaCl, 1.5 mM $NaN_3$, 0.3 mM DSS, 90% $H_2O$/10% $D_2O$ using standard experiments[58]. The longitudinal and transverse $^{15}$N relaxation rates R1 and R2, were collected with 12 and 14 data points, respectively, using corresponding delay times of 0.1 - 2 s and 4 -120 ms. The $^{15}$N-($^{1}$H) nuclear Overhauser ratios were obtained from a refence experiment without proton irradiation and a steady-state experiment with proton irradiation for 3 s.

The protomer interconversion rates in the 53BP1$^{TT}$-UNC2970 complex were determined using 2D longitudinal $^{1}$H-$^{15}$N-heteronuclear ZZ-exchange NMR spectroscopy[22-24]. For these experiments, a series of 11 spectra were acquired with mixing times of 0, 100, 200, 300, 400, 500, 600, 700, 800, 900, and 1000 ms in 25 mM sodium phosphate, pH 7.0, 100 mM NaCl, 1.5 mM $NaN_3$, 0.3 mM DSS, 90% $H_2O$/10% $D_2O$. The interconversion rates were obtained from nonlinear fitting of auto peak and exchange peak intensities accounting for two-site exchange

and $^{15}$N R1 relaxation using the equations previously described for a two-state model[24].

**X-ray crystallography**

Crystals of 53BP1$^{TT}$-PN mutant (40 mg/mL) were obtained by the hanging drop vapor diffusion method, mixing 1 μL of the sample in buffer 1 (50 mM sodium phosphate, pH 7.5, 50 mM NaCl) and 1 μL of the reservoir solution at 22 °C. Crystals of 53BP1$^{TT}$ WT (40 mg/mL) in complex with 14 mM of UNC3474, UNC3351, and UNC2991 molecules (all in buffer 1) and crystals of 53BP1$^{TT}$-CC mutant (15 mg/mL) in buffer 3 (50 mM Tris-HCl, pH 7.0, 100 mM NaCl) were obtained similarly. The reservoir solutions that produced crystals were: 1.5 M sodium/potassium phosphate, pH 6.0 (for free 53BP1$^{TT}$-PN); 2 M sodium formate, 0.1 M Bis-tris propane, pH 7.0 (for 53BP1$^{TT}$-UNC3474); 0.1 M sodium citrate tribasic, pH 5.6, 1 M ammonium phosphate monobasic (for 53BP1$^{TT}$-UNC3351); 1 M sodium formate, 0.1 M Bis-tris propane, pH 7.0 (for 53BP1$^{TT}$-UNC2991); and 0.1 M Bis-Tris, pH 6.5 (for 53BP1$^{TT}$-CC). Crystals of 53BP1$^{TT}$-CC were cryoprotected with 25% (w/v) xylitol. All other crystals were cryo-protected with 30% (v/v) glycerol.

Diffraction data for 53BP1$^{TT}$-PN and 53BP1$^{TT}$-UNC2991 were collected at the Cornel High Energy Synchrotron Source (beamline A1), while data for 53BP1$^{TT}$-UNC3474 (beamline 19-ID), 53BP1$^{TT}$-UNC3351 (beamline 19-ID), and 53BP1$^{TT}$-CC (beamline 19-BM) were collected at the Advanced Photon Source at Argonne National Laboratory. Diffraction data were processed with HKL2000. Phases were determined by molecular replacement using the crystal structure of 53BP1 tandem Tudor domain (PDB 2G3R[12]). Model building and refinement were carried out with COOT[59] and PHENIX[60]. All molecular representations were prepared with

ChimeraX[61].

**Small angle X-ray scattering (SAXS)**

SAXS measurements were performed at 10 °C and different concentrations (2, 4 and 6 mg/mL) of 53BP1$^{TT}$ WT, free and in complex with 10-fold molar excess of UNC3474 or UNC1118, in buffer 2 (25 mM sodium phosphate, pH 7.5, 15 mM NaCl), as well as on control samples containing only the small molecule in buffer 3. SAXS data were collected at the Lawrence Berkeley National Laboratory SYBILS beamline 12.3.1 and analyzed using programs from the SAXS data analysis software ATSAS (version 2.4.2) [62,63] including PRIMUS, GNOM, AUTOPOROD, GASBOR and CRYSOL. PRIMUS (version 3.0) was used for initial data processing. Radii of gyration ($R_g$) were calculated using the Guinier approximation[64]. Distance distribution functions $P$(r) and maximum particle dimensions were computed using GNOM. Molecular volumes and weights were estimated using AUTOPOROD. *Ab initio* reconstructions of molecular envelopes were done using GASBOR 2.3i. CRYSOL was used to back calculate the scattering curves and determine the goodness of fit.

**Isothermal titration calorimetry (ITC)**

The ITC measurements were performed at 25 °C using a MicroCal iTC200 calorimeter. 53BP1$^{TT}$ and the small molecules (UNC2991, UNC3351, UNC3474) were in 50 mM Tris-HCl, pH 7.5, 50 mM NaCl. In a typical run, 53BP1$^{TT}$ was in the reaction cell at a concentration of 150 to 160 μM while the small molecule, in the titration syringe at a concentration of 0.8 to 2 mM, was delivered as 2 μL injections every 3 min. The titrations were paired with control experiments for

heat of dilution. The titration of $53BP1^{TT}$ with UNC1118 was performed using a MicroCal VP-ITC calorimeter. ITC data were fitted to a one-site model using a Levenberg-Marquardt non-linear regression algorithm programmed in the Origin 7.0 software.

**Sedimentation velocity analytical ultracentrifugation (AUC)**

The AUC experiments were performed at 20 °C in 20 mM sodium phosphate, pH 7.5, with 50 mM NaCl. $53BP1^{TT}$ was at a concentration of 20 μM. Measurements were recorded on an Optima analytical ultracentrifuge (Beckman Coulter) with an An-50 Ti analytical 8-place rotor using absorbance detection at 280 nm. Sample-filled AUC cells assembled with 12-mm charcoal-filled Epon centerpieces and quartz windows were subjected to 3 h of equilibration at 20 °C under vacuum prior to initiating the experiments at 50,000 rpm with continuous data acquisition for 20 h (200 scans) at 20 °C. The AUC data were analyzed with the c(s) model in SEDFIT[65] using a partial specific volume of 0.7335 mL/g.

**Cell biology**

The focus-forming region (FFR; residues 1220-1711) of wild type 53BP1 and mutants E1549P/D1550N ($53BP1^{FFR}$-PN) and E1549C/E1566C ($53BP1^{FFR}$-CC) were inserted into the retroviral vector POZ. The $53BP1^{FFR}$ constructs were stably expressed at a moderate level in U2OS cells. To probe the effect of UNC3474 on $53BP1^{FFR}$ IRIF formation, U2OS cells were grown on glass coverslips, pre-incubated for 1 h with various concentrations of UNC3474 inhibitor and exposed to 1 Gy of X-ray radiation. After 1 h, the cells were fixed in 4% formaldehyde in PBS for 15 min at room temperature and blocked and permeabilized for 1 h in

PBS containing 0.3% Triton X-100, 1% BSA, 10% fetal bovine serum. For immunofluorescence, 53BP1$^{FFR}$ proteins (WT and 53BP1-PN) and γH2A.X were stained respectively with HA-Tag (C29F4) rabbit antibody (Cell Signaling Technology) and anti-γH2A.X (Ser139) (JBW301) mouse antibody (MilliporeSigma). Incubation with primary and secondary antibodies (Alexa Fluor, Molecular Probes) were done in PBS containing 1% BSA and 0.1% Triton X-100 for 1 h at room temperature. Coverslips were mounted using DAPI Fluoromount-G (Southern Biotech).

**Data availability**

The crystal structures have been deposited in the Protein Data Bank under accession codes 6MXX (53BP1$^{TT}$-UNC2991), 6MXY (53BP1$^{TT}$-UNC3351), 6MXZ (53BP1$^{TT}$-UNC3474), 6MY0 (53BP1$^{TT}$-PN), and 8FKH (53BP1$^{TT}$-CC).

**References**

1 Bunting, S. F. *et al.* 53BP1 inhibits homologous recombination in *Brca1*-deficient cells by blocking resection of DNA breaks. *Cell* **141**, 243-254 (2010).

2 Bouwman, P. *et al.* 53BP1 loss rescues BRCA1 deficiency and is associated with triple-negative and BRCA-mutated breast cancers. *Nat Struct Mol Biol* **17**, 688-695 (2010).

3 Zhao, W., Wiese, C., Kwon, Y., Hromas, R. & Sung, P. The BRCA tumor suppressor network in chromosome damage repair by homologous recombination. *Annu Rev Biochem* **88**, 221-245 (2019).

4 Witus, S. R., Stewart, M. D. & Klevit, R. E. The BRCA1/BARD1 ubiquitin ligase and its

substrates. *Biochem J* **478**, 3467-3483 (2021).

5 Densham, R. M. *et al.* Human BRCA1-BARD1 ubiquitin ligase activity counteracts chromatin barriers to DNA resection. *Nat Struct Mol Biol* **23**, 647-655 (2016).

6 Mattiroli, F. & Penengo, L. Histone ubiquitination: An integrative signaling platform in genome stability. *Trends Genet* **37**, 566-581 (2021).

7 Fradet-Turcotte, A. *et al.* 53BP1 is a reader of the DNA-damage-induced H2A Lys 15 ubiquitin mark. *Nature* **499**, 50-54 (2013).

8 Wilson, M. D. *et al.* The structural basis of modified nucleosome recognition by 53BP1. *Nature* **536**, 100-103 (2016).

9 Becker, J. R. *et al.* BARD1 reads H2A lysine 15 ubiquitination to direct homologous recombination. *Nature* **596**, 433-437 (2021).

10 Hu, Q. *et al.* Mechanisms of BRCA1-BARD1 nucleosome recognition and ubiquitylation. *Nature* **596**, 438-443 (2021).

11 Dai, L. *et al.* Structural insight into BRCA1-BARD1 complex recruitment to damaged chromatin. *Mol Cell* **81**, 2765-2777 e2766 (2021).

12 Botuyan, M. V. *et al.* Structural basis for the methylation state-specific recognition of histone H4-K20 by 53BP1 and Crb2 in DNA repair. *Cell* **127**, 1361-1373 (2006).

13 Tang, J. *et al.* Acetylation limits 53BP1 association with damaged chromatin to promote homologous recombination. *Nat Struct Mol Biol* **20**, 317-325 (2013).

14 Nakamura, K. *et al.* H4K20me0 recognition by BRCA1-BARD1 directs homologous recombination to sister chromatids. *Nat Cell Biol* **21**, 311-318 (2019).

15 Perfetti, M. T. *et al.* Identification of a fragment-like small molecule ligand for the methyl-lysine binding protein, 53BP1. *ACS Chem Biol* **10**, 1072-1081 (2015).

16 Luo, J., Liu, Z., Guo, Y. & Li, M. A structural dissection of large protein-protein crystal packing contacts. *Sci Rep* **5**, 14214 (2015).

17 Charier, G. *et al.* The Tudor tandem of 53BP1: a new structural motif involved in DNA and RG-rich peptide binding. *Structure* **12**, 1551-1562 (2004).

18 Tong, Q. *et al.* Structural plasticity of methyllysine recognition by the tandem tudor domain of 53BP1. *Structure* **23**, 312-321 (2015).

19 Roy, S. *et al.* Structural insight into p53 recognition by the 53BP1 tandem Tudor domain. *J Mol Biol* **398**, 489-496 (2010).

20 Rambo, R. P. & Tainer, J. A. Super-resolution in solution X-Ray scattering and its applications to structural systems biology. *Annual review of biophysics* **42**, 415-441 (2013).

21 James, L. I. *et al.* Small-molecule ligands of methyl-lysine binding proteins: optimization of selectivity for L3MBTL3. *J Med Chem* **56**, 7358-7371 (2013).

22 Farrow, N. A., Zhang, O., Forman-Kay, J. D. & Kay, L. E. Comparison of the backbone dynamics of a folded and an unfolded SH3 domain existing in equilibrium in aqueous buffer. *Biochemistry* **34**, 868-878 (1995).

23 Tyler, R. C., Wieting, J. C., Peterson, F. C. & Volkman, B. F. Electrostatic optimization of the conformational energy landscape in a metamorphic protein. *Biochemistry* **51**, 9067-9075 (2012).

24 Zhang, Y. *et al.* High pressure ZZ-exchange NMR reveals key features of protein folding

transition states. *J Am Chem Soc* **138**, 15260-15266 (2016).

25 Mer, G., Kellenberger, E. & Lefèvre, J. F. Alpha-helix mimicry of a beta-turn. *J Mol Biol* **281**, 235-240 (1998).

26 Craig, D. B. & Dombkowski, A. A. Disulfide by Design 2.0: A web-based tool for disulfide engineering in proteins. *BMC Bioinformatics* **14**, 346 (2013).

27 Iwabuchi, K. *et al.* Potential role for 53BP1 in DNA end-joining repair through direct interaction with DNA. *J Biol Chem* **278**, 36487-36495 (2003).

28 Drané, P. *et al.* TIRR regulates 53BP1 by masking its histone methyl-lysine binding function. *Nature* **543**, 211-216 (2017).

29 Dos Santos Passos, C., Choi, Y. S., Snow, C. D., Yao, T. & Cohen, R. E. Design of genetically encoded sensors to detect nucleosome ubiquitination in live cells. *J Cell Biol* **220** (2021).

30 Go, Y. M. & Jones, D. P. Redox compartmentalization in eukaryotic cells. *Biochim Biophys Acta* **1780**, 1273-1290 (2008).

31 Go, Y. M. & Jones, D. P. Redox control systems in the nucleus: Mechanisms and functions. *Antioxid Redox Signal* **13**, 489-509 (2010).

32 Patwardhan, R. S., Sharma, D. & Sandur, S. K. Thioredoxin reductase: An emerging pharmacologic target for radiosensitization of cancer. *Transl Oncol* **17**, 101341 (2022).

33 Maurer-Stroh, S. *et al.* The Tudor domain 'Royal Family': Tudor, plant Agenet, Chromo, PWWP and MBT domains. *Trends Biochem Sci* **28**, 69-74 (2003).

34 Linhares, B. M., Grembecka, J. & Cierpicki, T. Targeting epigenetic protein-protein

interactions with small-molecule inhibitors. *Future Med Chem* **12**, 1305-1326 (2020).

35 Arrowsmith, C. H. & Schapira, M. Targeting non-bromodomain chromatin readers. *Nat Struct Mol Biol* **26**, 863-869 (2019).

36 James, L. I. *et al.* Discovery of a chemical probe for the L3MBTL3 methyllysine reader domain. *Nat Chem Biol* **9**, 184-191 (2013).

37 Adams, M. M. *et al.* 53BP1 oligomerization is independent of its methylation by PRMT1. *Cell Cycle* **4**, 1854-1861 (2005).

38 Ward, I. *et al.* The tandem BRCT domain of 53BP1 is not required for its repair function. *J Biol Chem* **281**, 38472-38477 (2006).

39 Zgheib, O., Pataky, K., Brugger, J. & Halazonetis, T. D. An oligomerized 53BP1 tudor domain suffices for recognition of DNA double-strand breaks. *Mol Cell Biol* **29**, 1050-1058 (2009).

40 Botuyan, M. V. *et al.* Mechanism of 53BP1 activity regulation by RNA-binding TIRR and a designer protein. *Nat Struct Mol Biol* **25**, 591-600 (2018).

41 Sundaravinayagam, D. *et al.* 53BP1 supports immunoglobulin class switch recombination independently of its DNA double-strand break end protection function. *Cell Rep* **28**, 1389-1399 e1386 (2019).

42 Zhang, A., Peng, B., Huang, P., Chen, J. & Gong, Z. The p53-binding protein 1-Tudor-interacting repair regulator complex participates in the DNA damage response. *J Biol Chem* **292**, 6461-6467 (2017).

43 Dai, Y., Zhang, A., Shan, S., Gong, Z. & Zhou, Z. Structural basis for recognition of 53BP1 tandem Tudor domain by TIRR. *Nat Commun* **9**, 2123 (2018).

44 Wang, J. *et al.* Molecular basis for the inhibition of the methyl-lysine binding function of 53BP1 by TIRR. *Nat Commun* **9**, 2689 (2018).

45 Parnandi, N. *et al.* TIRR inhibits the 53BP1-p53 complex to alter cell-fate programs. *Mol Cell* **81**, 2583-2595 e2586 (2021).

46 Canny, M. D. *et al.* Inhibition of 53BP1 favors homology-dependent DNA repair and increases CRISPR-Cas9 genome-editing efficiency. *Nat Biotechnol* **36**, 95-102 (2018).

47 Nambiar, T. S. *et al.* Stimulation of CRISPR-mediated homology-directed repair by an engineered RAD18 variant. *Nat Commun* **10**, 3395 (2019).

48 Maleki Dana, P., Sadoughi, F., Mirzaei, H., Asemi, Z. & Yousefi, B. DNA damage response and repair in the development and treatment of brain tumors. *Eur J Pharmacol* **924**, 174957 (2022).

49 Squatrito, M., Vanoli, F., Schultz, N., Jasin, M. & Holland, E. C. 53BP1 is a haploinsufficient tumor suppressor and protects cells from radiation response in glioma. *Cancer Res* **72**, 5250-5260 (2012).

50 Zhang, T., Chai, J. & Chi, L. Induction of XLF and 53BP1 expression is associated with temozolomide resistance In glioblastoma cells. *Onco Targets Ther* **12**, 10139-10151 (2019).

51 Cui, G., Botuyan, M. V. & Mer, G. Preparation of recombinant peptides with site- and degree-specific lysine $^{13}$C-methylation. *Biochemistry* **48**, 3798-3800 (2009).

52 Mallette, F. A. *et al.* RNF8- and RNF168-dependent degradation of KDM4A/JMJD2A triggers 53BP1 recruitment to DNA damage sites. *EMBO J* **31**, 1865-1878 (2012).

53 Cui, G. *et al.* PHF20 is an effector protein of p53 double lysine methylation that stabilizes

and activates p53. *Nat Struct Mol Biol* **19**, 916-924 (2012).

54 Delaglio, F. *et al.* NMRPipe: a multidimensional spectral processing system based on UNIX pipes. *J Biomol NMR* **6**, 277-293 (1995).

55 Johnson, B. A. & Blevins, R. A. NMRView: A computer program for visualization and analysis of NMR data. *J Biomol NMR* **4**, 603-614 (1994).

56 Johnson, B. A. From raw data to protein backbone chemical shifts using NMRFx processing and NMRViewJ analysis. *Methods Mol Biol* **1688**, 257-310 (2018).

57 Ferentz, A. E. & Wagner, G. NMR spectroscopy: A multifaceted approach to macromolecular structure. *Q Rev Biophys* **33**, 29-65 (2000).

58 Dayie, K. T., Wagner, G. & Lefèvre, J. F. Theory and practice of nuclear spin relaxation in proteins. *Annu Rev Phys Chem* **47**, 243-282 (1996).

59 Emsley, P. & Cowtan, K. Coot: model-building tools for molecular graphics. *Acta crystallogr D Biol Crystallogr* **60**, 2126-2132 (2004).

60 Adams, P. D. *et al.* PHENIX: a comprehensive Python-based system for macromolecular structure solution. *Acta Crystallogr D Biol Crystallogr* **66**, 213-221 (2010).

61 Goddard, T. D. *et al.* UCSF ChimeraX: Meeting modern challenges in visualization and analysis. *Protein Sci* **27**, 14-25 (2018).

62 Petoukhov, M. V. *et al.* New developments in the ATSAS program package for small-angle scattering data analysis. *J Appl Cryst* **45**, 342-350 (2012).

63 Franke, D. *et al.* ATSAS 2.8: a comprehensive data analysis suite for small-angle scattering from macromolecular solutions. *J Appl Crystallogr* **50**, 1212-1225 (2017).

64 Guinier, A. & Fournet, G. *Small-angle scattering of X-rays*. (John Wiley and Sons, 1955).

65 Schuck, P. Size-distribution analysis of macromolecules by sedimentation velocity ultracentrifugation and lamm equation modeling. *Biophys J* **78**, 1606-1619 (2000).

**Acknowledgements**

We are very grateful to Nicolas Foloppe for insightful discussions and advice, to Kemin Tan at Argonne National Laboratory Advanced Photon Source (APS) for assistance with X-ray data collection and to Greg Hura at Lawrence Berkeley National Laboratory Advanced Light Source (ALS) for assistance with SAXS data collection. This research was supported by the US National Institutes of Health (NIH) awards R35 GM136262 and R01 CA132878 to G.M., US Department of Defense Ovarian Cancer Research Program awards W81XWH-16-1-0391 and W81XWH-20-1-0322 to M.V.B. and G.M., and NIH grants R01 CA208244 and R01 CA264900 and Gray Foundation Team Science Award to D.C. X-ray crystallography data were collected at the APS Structural Biology Center funded by the U.S. Department of Energy (DOE), Office of Biological and Environmental Research and operated for the DOE Office of Science by Argonne National Laboratory under contract DE-AC02-06CH11357. X-ray crystallography data were also collected at the Cornell High-Energy Synchrotron Source (CHESS), which is supported by the National Science Foundation under award DMR-1829070, and the Macromolecular Diffraction at CHESS (MacCHESS) facility, which is supported by NIH award P30 GM124166. The SAXS data were collected at the ALS SIBYLS beamline, supported by the DOE, Office of Biological Environmental Research, and by the NIH project ALS-ENABLE (P30 GM124169) and High-End Instrumentation Grant S10 OD018483.

**Author contributions**

Conceptualization, G.M., G. C., and M. V. B.; Investigation, G. C., M. V. B., P. D., Q. H., B. B., J. R. T., D. J. S., A.D., M. T. P., L. I. J., and G. M.; Writing—original draft, G. M. and M. V. B.; Writing—review and editing, G. M., M. V. B., J. R. T., G. C., P. D., D. J. S., L. I. J. and S. V. F.; Supervision, G. M. and D. C.

**Competing interests**

The authors declare no competing interests.

**Figures**

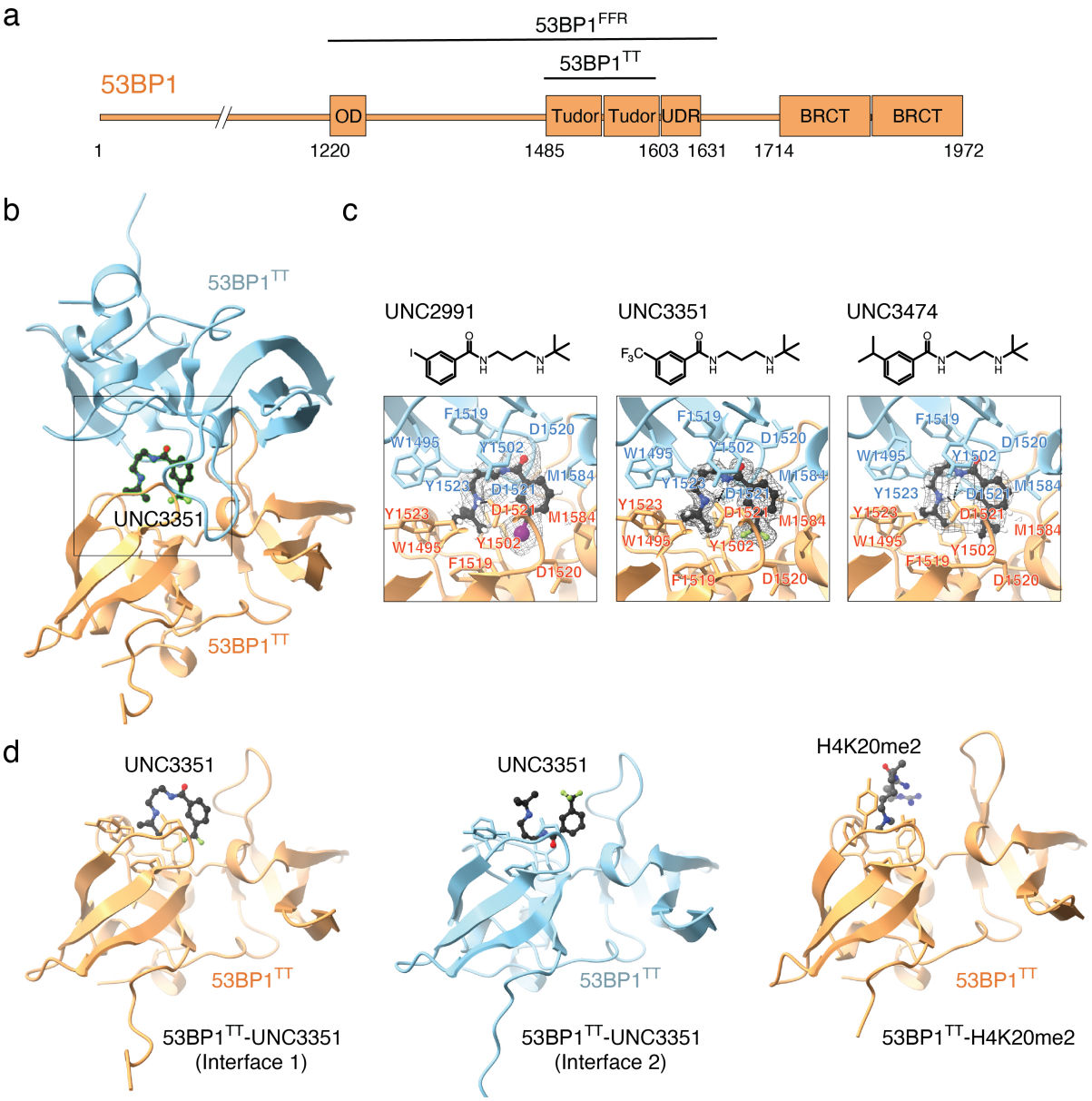


**Figure 1 | Interaction of 53BP1$^{TT}$ with small molecules probed using X-ray crystallography.**

**a**, Domain structure of 53BP1. OD stands for oligomerization domain and UDR for ubiquitin-dependent recognition motif. 53BP1$^{TT}$ is the tandem Tudor domain of 53BP1. 53BP1$^{FFR}$ is the minimal foci-forming region of 53BP1.

**b**, Crystal structure showing the encapsulation of UNC3351 by two 53BP1$^{TT}$ molecules.

**c**, Binding interfaces of UNC2991, UNC3351 and UNC3474 with $53BP1^{TT}$ in the crystal structures of their complexes. The 2mFo-DFc electron density maps contoured at 1σ level are shown as gray mesh around each compound.

**d**, Binding interfaces in the structure of $53BP1^{TT}$ bound to UNC3351 (left and middle panels) and to an H4K20me2 peptide[12] (right panel). The side chains in the binding cage of $53BP1^{TT}$ are shown.

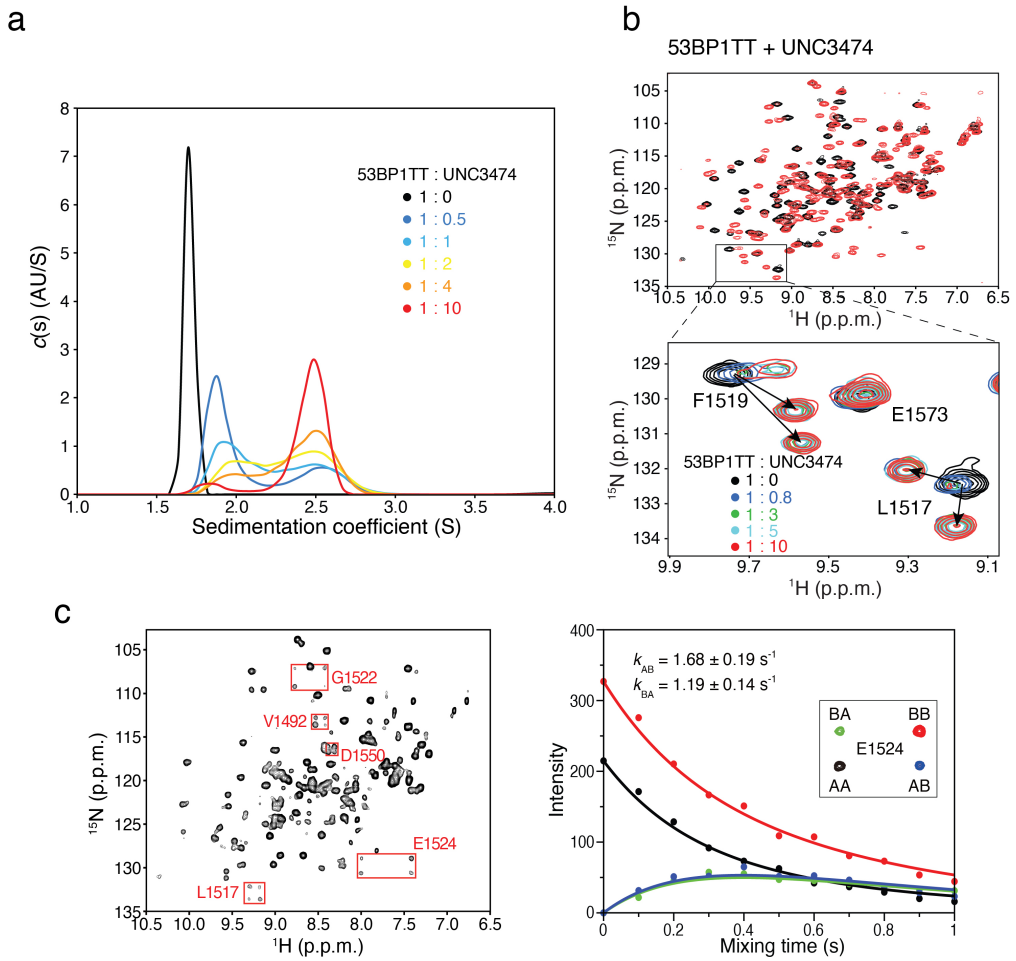


**Figure 2 | Oligomerization of 53BP1$^{TT}$-UNC3474 probed using analytical ultracentrifugation (AUC) and NMR spectroscopy.**

**a**, Sedimentation velocity analysis of 53BP1$^{TT}$ (20 μM) at different concentrations of UNC3474 using AUC. The sedimentation coefficient distributions are shown for free 53BP1$^{TT}$ (black) and for 53BP1$^{TT}$ at increasing concentrations of UNC3474; 10 μM (blue), 20 μM (light blue), 40 μM (yellow), 80 μM (orange) and 200 μM (red).

**b**, Top: Overlay of $^{1}$H-$^{15}$N HSQC NMR spectra of $^{15}$N-labeled 53BP1$^{TT}$, free (black) and bound to UNC3474 (red). Bottom: Examples of doubling of resonances (L1517 and F1519 signals) at different 53BP1$^{TT}$:UNC3474 molar ratios.

**c**. $^{1}$H-$^{15}$N-heteronuclear ZZ-exchange NMR spectroscopy of the interaction of 53BP1$^{TT}$ with UNC2170 at 25 °C using 1 mM $^{15}$N-labeled 53BP1$^{TT}$ and 9 mM UNC2170. Fitting was done for the signals of E1524 (inset). The black and red curves show the decay of the auto peaks (AA and BB) and blue and green curves show the buildup and decay of the exchange peaks (AB and BA). The interconversion rates are indicated.

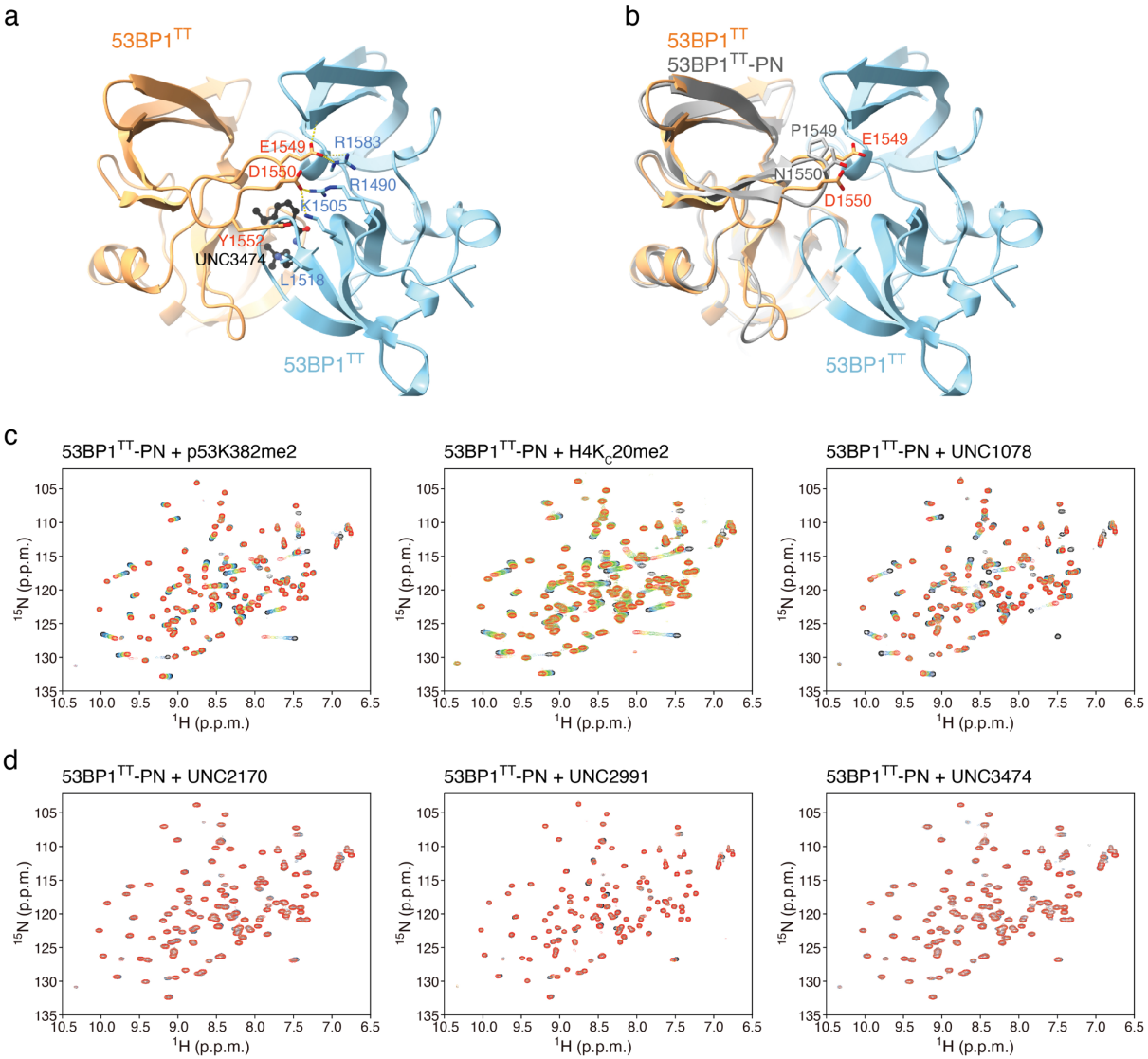


**Figure 3 | Small molecules stabilize a pre-existing lowly populated 53BP1$^{TT}$ homodimer.**

**a**, Key inter-53BP1$^{TT}$ contacts in the structure of 53BP1$^{TT}$-UNC3474 complex. Hydrogen bonds and salt bridges are represented by yellow dashed lines.

**b**, Structural overlay of wild type 53BP1$^{TT}$ and mutant 53BP1$^{TT}$-PN in which E1549 and D1550 are replaced by a proline and an asparagine, respectively.

**c**, NMR spectroscopy-monitored titration of $^{15}$N-labeled 53BP1$^{TT}$-PN with non-labeled H4K$_C$20me2 and p53K382me2 peptides and small molecule UNC1078. Shown in different

colors are the overlaid $^{1}H$-$^{15}N$ HSQC spectra of 53BP1$^{TT}$-PN recorded without (black) and with increasing amounts of added compounds, up to 4-fold molar excess (red).

**d**, Same as **c** but for the titration of 53BP1$^{TT}$-PN with small molecules UNC2170, UNC2991 and UNC3474.

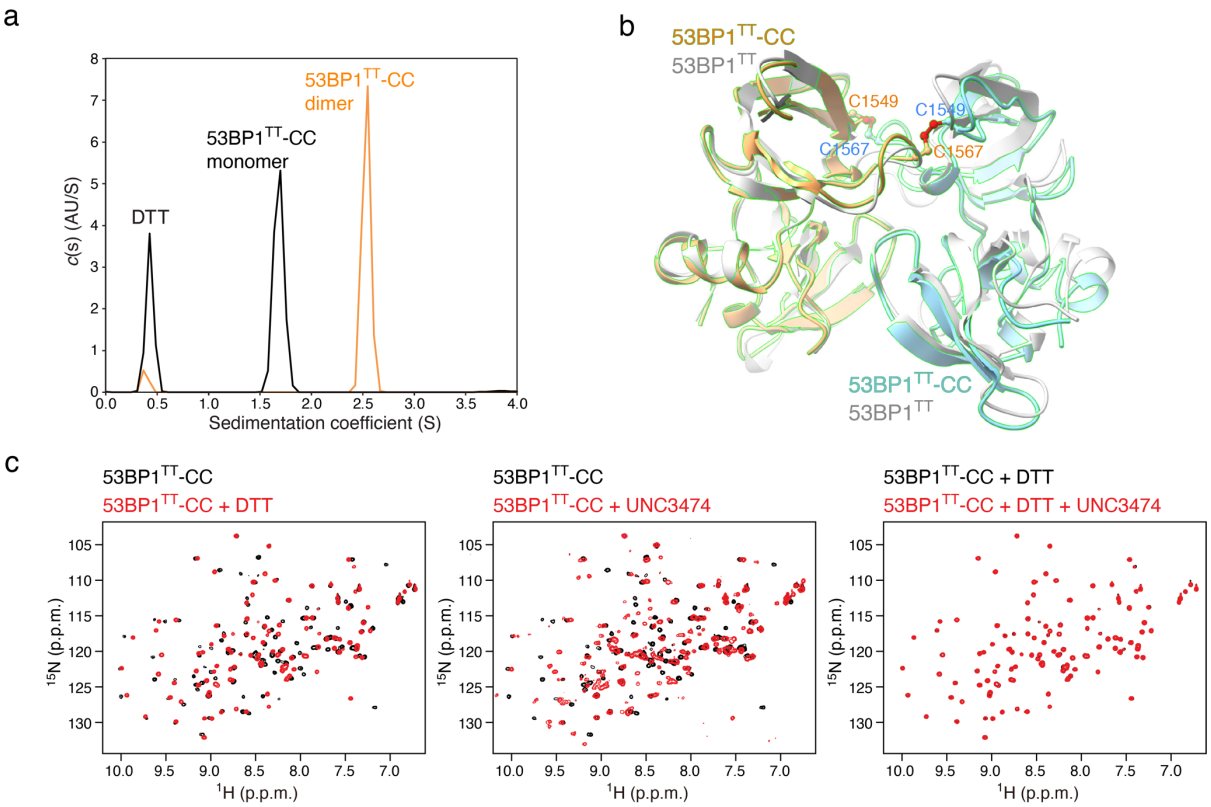


**Figure 4 | Engineering of a disulfide-crosslinked 53BP1$^{TT}$ homodimer that binds UNC3474.**

**a**, Sedimentation velocity analysis of 53BP1$^{TT}$-CC (20 μM) in the presence and absence of 10 mM DTT.

**b**, Crystal structure of 53BP1$^{TT}$-CC (blue and orange) showing the two disulfide bridges overlaid to the crystal structure of 53BP1$^{TT}$-UNC3474 (UNC3474 omitted) in gray.

**c**, Effects of adding 2 mM DTT and UNC3474 on the $^{1}$H-$^{15}$N HSQC spectrum of $^{15}$N-labeled 53BP1$^{TT}$-CC (1:1 UNC3474:53BP1$^{TT}$-CC molar ratio).

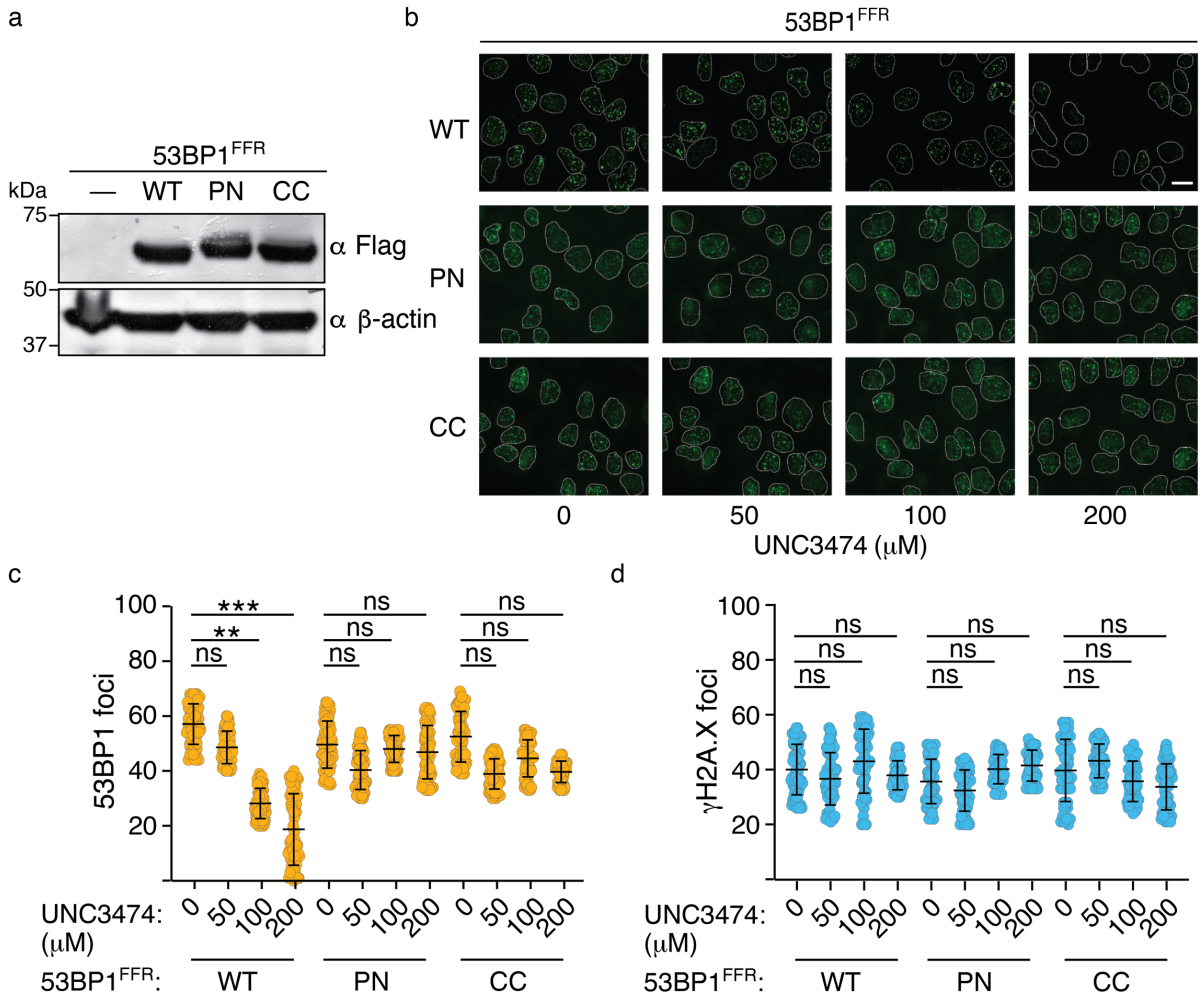


**Figure 5 | Demonstration of an autoinhibited state for 53BP1 chromatin recruitment in cells using UNC3474 as a chemical probe.**

**a**, Immunoblotting showing the expression of the indicated 53BP1$^{FFR}$ construct in stably transfected U2OS cells. β-actin staining was used as control.

**b**, Representative data for the effect of UNC3474 on IRIF formation by WT 53BP1$^{FFR}$, 53BP1$^{FFR}$-PN and 53BP1$^{FFR}$-CC after cell exposure to 1 Gy of X-ray radiation. Scale bar represents 10 μm.

**c**, Effect of UNC3474 on WT 53BP1$^{FFR}$, 53BP1$^{FFR}$-PN and 53BP1$^{FFR}$-CC IRIF number (mean ±

s.d., n = 3).

**d**, Number of γH2A.X IRIF for the cells analyzed in **c** (mean ± s.d., n = 3). Labels *, ** and *** indicate $P < 0.05$, $P < 0.01$ and $P < 0.001$, respectively. In c and d, $P$ values were calculated using a two-tailed $t$-test. ns stands for not significant.

**Table 1 Data collection and refinement statistics**

| | 53BP1$^{TT}$-UNC2991 (PDB 6MXX) | 53BP1$^{TT}$-UNC3351 (PDB 6MXY) | 53BP1$^{TT}$-UNC3474 (PDB 6MXZ) | 53BP1$^{TT}$-PN (PDB 6MY0) | 53BP1$^{TT}$-CC (PDB 8FKH) |
|---|---|---|---|---|---|
| **Data collection** | | | | | |
| Space group | $P2_1\,2_1\,2_1$ | $P3_121$ | $P2_12_12_1$ | $C2\,2\,2_1$ | $P2_1\,2_1\,2_1$ |
| Cell dimensions | | | | | |
| *a*, *b*, *c* (Å) | 68.94, 159.43, 181.19 | 60.57, 60,57, 138.22 | 68.67, 160.71, 182.65 | 73.10,141.27, 47.06 | 72.50, 161.83, 179.95 |
| $\alpha, \beta, \gamma$ (°) | 90, 90, 90 | 90, 90, 120 | 90, 90, 90 | 90, 90, 90 | 90, 90, 90 |
| Resolution (Å) | 50-2.30 (2.38-2.30)* | 50-1.62 (1.68-1.62) | 50-2.50 (2.59-2.50) | 50-2.20 (2.28-2.20) | 50-3.79 (3.92-3.79) |
| $R_{merge}$ | 0.077 (1.06) | 0.074 (0.741) | 0.045 (0.436) | 0.087 (0.55) | 0.120 (0.621) |
| $I/\sigma I$ | 21.3 (1.3) | 30.6 (2.7) | 20.5 (2.4) | 23.4 (5.3) | 15.7 (3.2) |
| Completeness (%) | 97.5 (75.3) | 99.7 (98.0) | 97.2 (76.4) | 98.6 (87.4) | 89.5 (75.1) |
| Redundancy | 14.0 (6.7) | 11.2 (8.0) | 6.0 (6.1) | 12.2 (11.4) | 5.7 (5.0) |
| **Refinement** | | | | | |
| Resolution (Å) | 48.14-2.30 | 18.48-1.62 | 17.60-2.50 | 39.60-2.20 | 48.19-3.79 |
| No. of unique reflections | 87459 | 37781 | 68884 | 12596 | 19548 |
| $R_{work}$ / $R_{free}$ | 0.206 / 0.232 | 0.179 / 0.213 | 0.191 / 0.223 | 0.187 / 0.233 | 0.279 / 0.327 |
| No. atoms | | | | | |
| Protein | 10054 | 1996 | 10562 | 1887 | 8405 |
| Ligand/ion | 297 | 46 | 221 | 129 | N/A |
| Water | 411 | 348 | 667 | 240 | N/A |
| *B*-factors | | | | | |
| Protein | 55.90 | 19.77 | 56.25 | 27.71 | 106.76 |
| Ligand/ion | 124.93 | 43.04 | 49.13 | N/A | N/A |
| Water | 48.00 | 31.33 | 49.02 | 31.13 | N/A |
| R.m.s. deviations | | | | | |
| Bond lengths (Å) | 0.004 | 0.019 | 0.003 | 0.004 | 0.004 |
| Bond angles (°) | 0.93 | 1.71 | 0.93 | 0.97 | 0.91 |

[a]Values in parentheses are for highest-resolution shell.

# Supplementary Information

## An autoinhibited state of 53BP1 revealed by small molecule antagonists and protein engineering

Gaofeng Cui[1,*], Maria Victoria Botuyan[1,*], Pascal Drané[2,*], Qi Hu[1], Benoît Bragantini[1], James R. Thompson[3], David J. Schuller[4], Alexandre Detappe[5], Michael T. Perfetti[6], Lindsey I. James[6,7], Stephen V. Frye[6,7], Dipanjan Chowdhury[2] and Georges Mer[1,8,#]

*Equal contributions

[#]Correspondence: mer.georges@mayo.edu

## Extended Data Figures

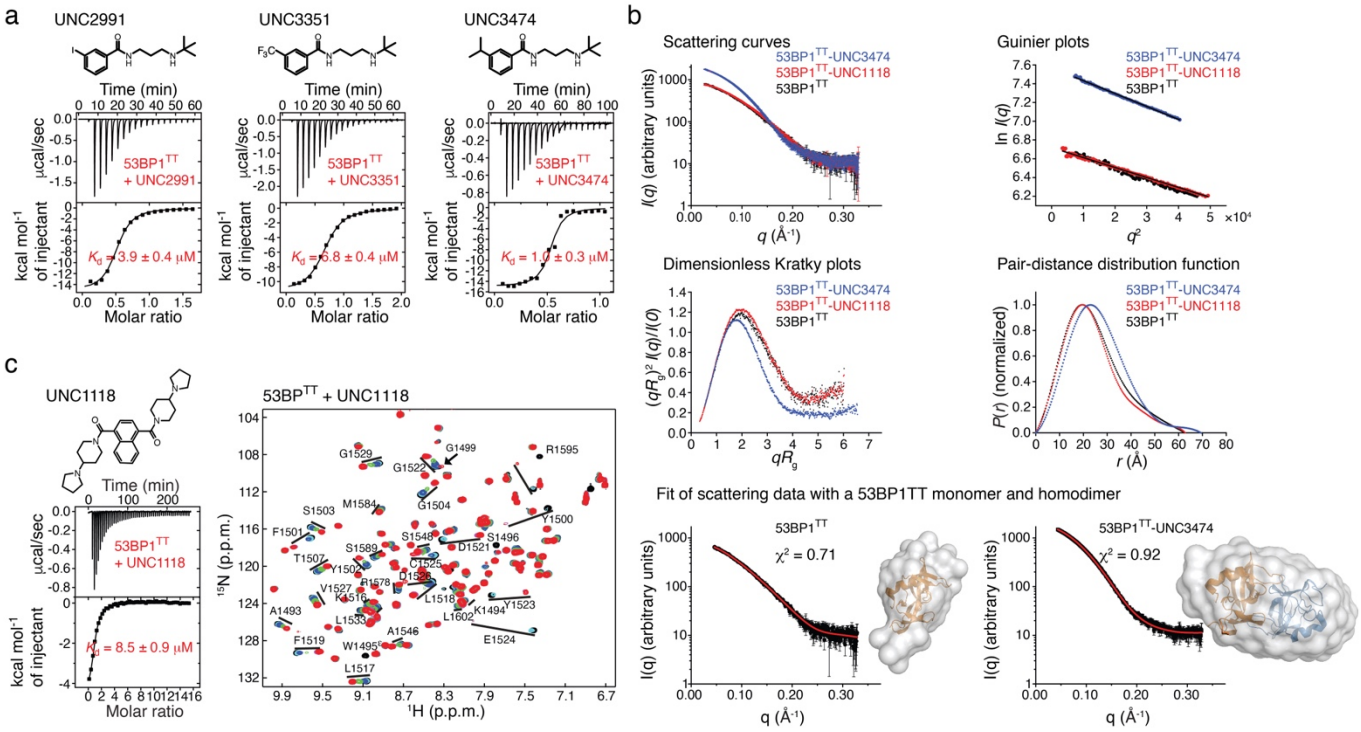


**Extended Data Figure 1 | Interaction of 53BP1$^{TT}$ with small molecules probed using isothermal titration calorimetry (ITC) and small-angle X-ray scattering (SAXS).**

**a**, ITC of the interaction of UNC2991, UNC3351 and UNC3474 with 53BP1$^{TT}$. Raw titration data and integrated heat measurements are shown. Indicated apparent $K_d$s with associated standard deviations were determined by nonlinear least-squares analysis.

**b**, SAXS curves for 53BP1$^{TT}$, 53BP1$^{TT}$-UNC1118 and 53BP1$^{TT}$-UNC3474. Two mg/mL of 53BP1$^{TT}$ was used, without and with 10-fold molar excess of UNC1118 or UNC3474. The Guinier plots, dimensionless Kratky plots and pair distance distribution functions derived from the SAXS data are shown. Also shown are the crystal structures of 53BP1$^{TT}$ and 53BP1$^{TT}$-UNC3474 overlaid to the corresponding SAXS-based *ab initio* molecular envelopes generated using DAMMIF.

**c**, Interaction of UNC1118 with 53BP1$^{TT}$ characterized using ITC (left) and NMR spectroscopy (right). For the ITC, raw titration data and integrated heat measurements are shown. The indicated $K_d$ with associated standard deviation was determined by nonlinear least-squares analysis.

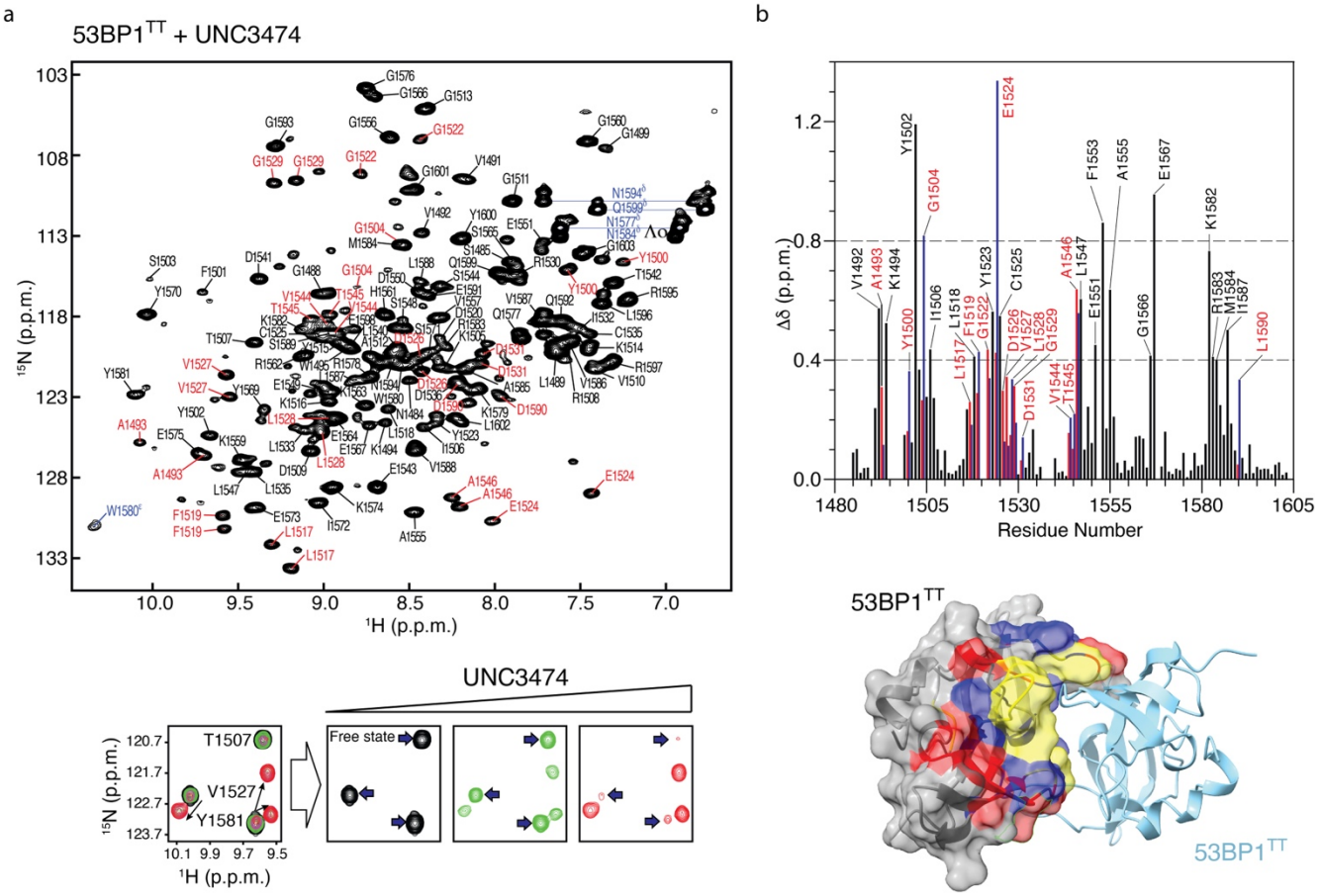


**Extended Data Figure 2 | Interaction of 53BP1$^{TT}$ with small molecules probed using NMR spectroscopy.**

**a**, Top: Assigned $^{1}$H-$^{15}$N HSQC spectrum of $^{15}$N-labeled 53BP1$^{TT}$ bound to non-labeled UNC3474 at a 53BP1$^{TT}$:UNC3474 molar ratio of 1:10. Residues for which there is doubling of resonances are labeled in red. The $^{1}$H-$^{15}$N resonances for the asparagine and glutamine side chain amide groups and tryptophan indole ring are labeled in blue. Bottom: Changes in NMR signal positions for three residues in the $^{1}$H-$^{15}$N HSQC spectrum of $^{15}$N-labeled 53BP1$^{TT}$ upon titration with non-labeled UNC3474 highlighting the slow exchange on the chemical shift time scale.

**b**, Top: Chemical shift perturbations ($\Delta\delta$) in $^{15}$N-labeled 53BP1$^{TT}$ at 10-fold molar excess of non-labeled UNC3474. Black bars are for residues with $\Delta\delta > 0.4$. Blue and red bars are for residues with split signals. Bottom: Mapping of chemical shift perturbations on the surface and ribbon representation of one of the two protomers in the 53BP1$^{TT}$-UNC3474 structure (UNC3474 omitted). Residues with $\Delta\delta > 0.4$ are colored blue and those with split signals are colored red. Residues for which signals are missing due to exchange broadening are colored yellow.

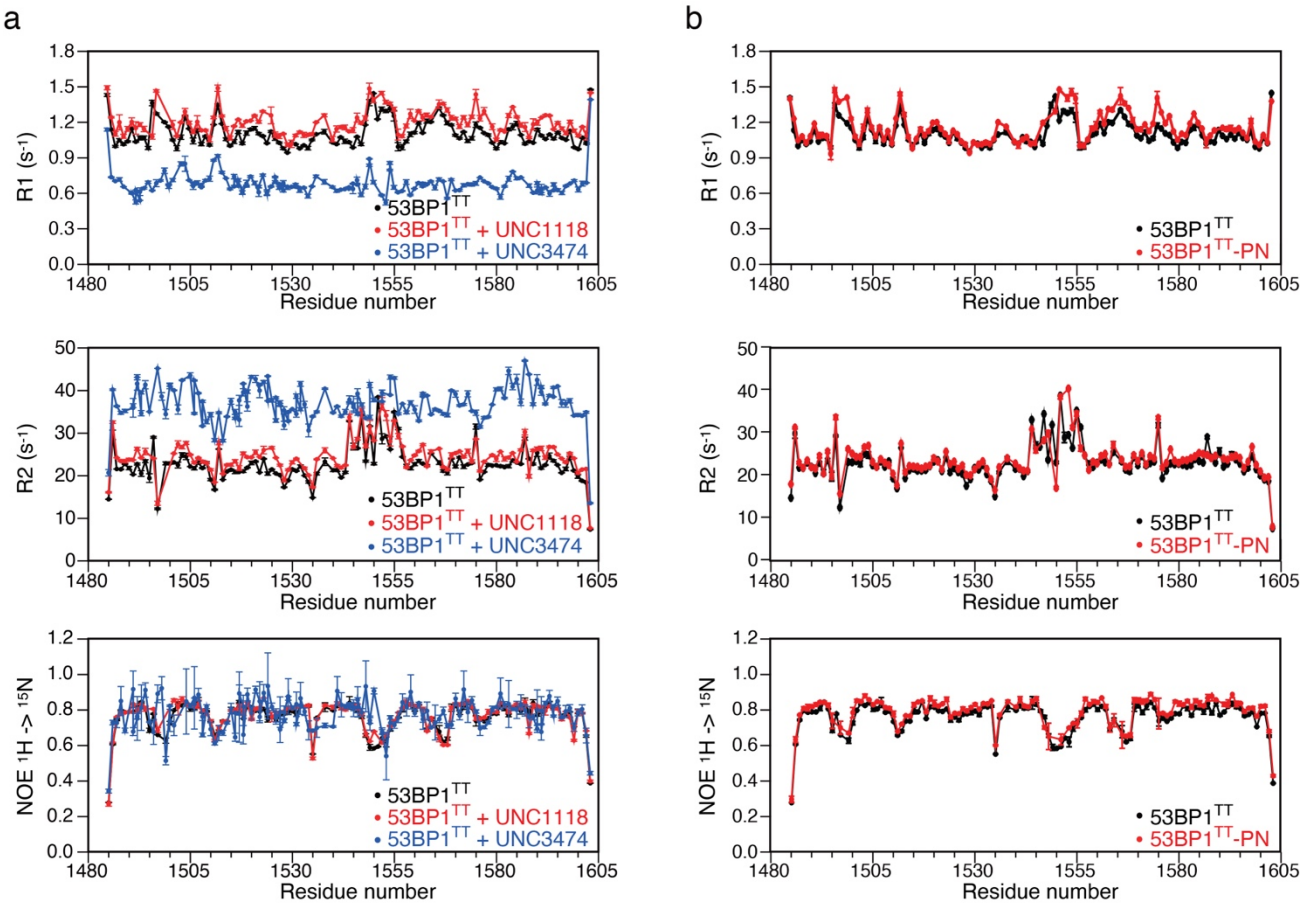


**Extended Data Figure 3 | NMR relaxation measurements.**

**a**, NMR relaxation values for 53BP1$^{TT}$ without and with 9-fold molar excess each of UNC3474 and UNC1118.

**b**, NMR relaxation values for 53BP1$^{TT}$ and 53BP1$^{TT}$-PN, both in free states.

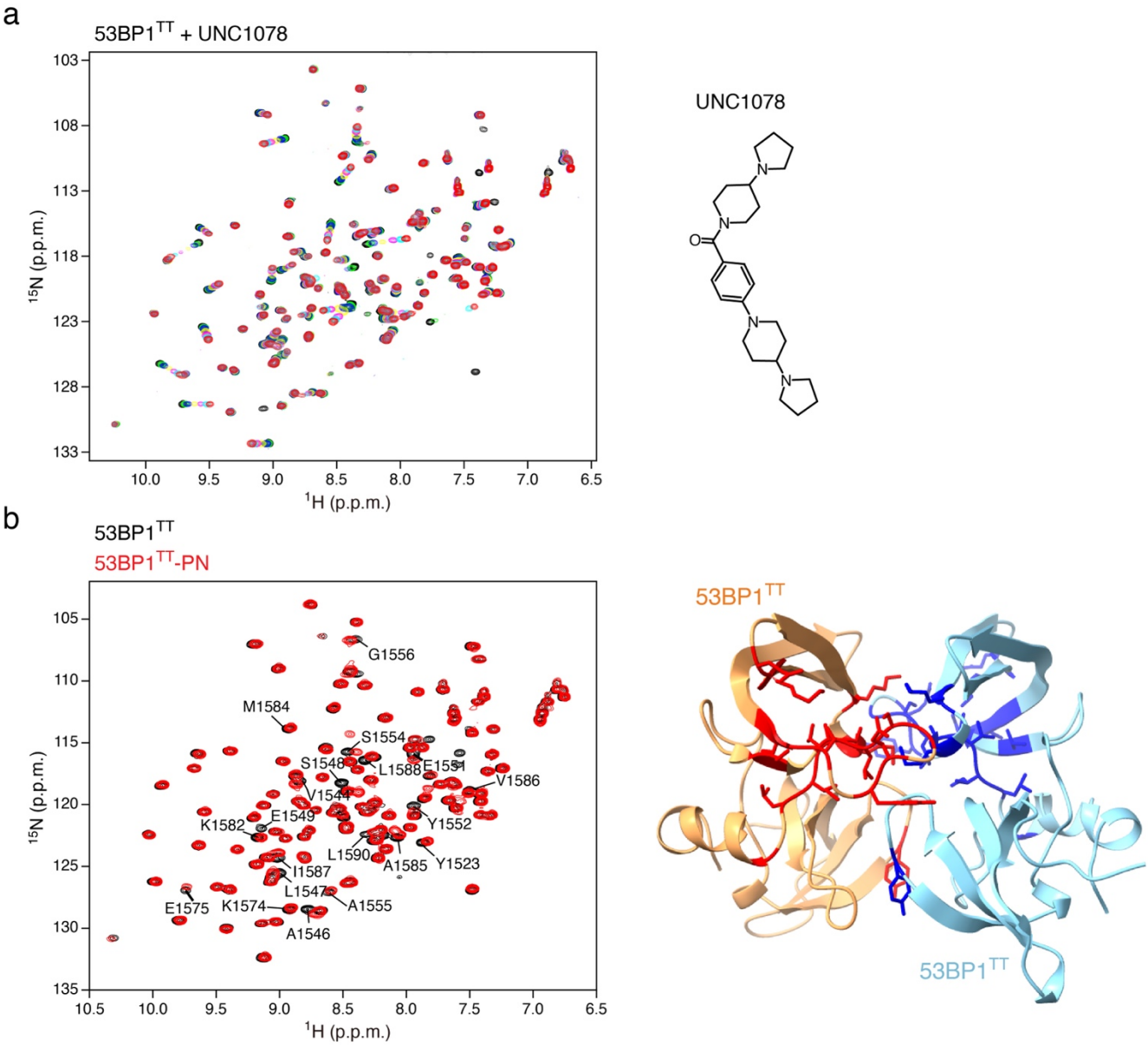


**Extended Data Figure 4 | Comparative NMR spectroscopy of 53BP1$^{TT}$ and 53BP1$^{TT}$-PN.**

**a**, NMR spectroscopy-monitored interaction of 53BP1$^{TT}$ with UNC1078. Shown in different colors are the overlaid $^{1}$H-$^{15}$N HSQC spectra of 53BP1$^{TT}$ recorded without (black) and with increasing amounts of UNC1078, up to 4-fold molar excess (red).

**b**, Overlay of the $^{1}$H-$^{15}$N HSQC spectra of 53BP1$^{TT}$ and 53BP1-$^{TT}$-PN. The two proteins were at a concentration of 0.3 mM. Residues for which the chemical shifts changed are labeled on the left. The residues are mapped (in red and blue colors) on the structure of the 53BP1$^{TT}$ homodimer bound to UNC3474 (UNC3474 omitted) on the right.